

A Novel Method to Derive Exospheric Temperatures from Swarm Thermospheric Densities during Quiet Times

Lin, Yingyun ; Xu, Jiyao; van den IJssel, J.A.A.; Yuan, Wei

DOI

[10.3390/rs14215382](https://doi.org/10.3390/rs14215382)

Publication date

2022

Document Version

Final published version

Published in

Remote Sensing

Citation (APA)

Lin, Y., Xu, J., van den IJssel, J. A. A., & Yuan, W. (2022). A Novel Method to Derive Exospheric Temperatures from Swarm Thermospheric Densities during Quiet Times. *Remote Sensing*, 14(21), Article 5382. <https://doi.org/10.3390/rs14215382>

Important note

To cite this publication, please use the final published version (if applicable). Please check the document version above.

Copyright

Other than for strictly personal use, it is not permitted to download, forward or distribute the text or part of it, without the consent of the author(s) and/or copyright holder(s), unless the work is under an open content license such as Creative Commons.

Takedown policy

Please contact us and provide details if you believe this document breaches copyrights. We will remove access to the work immediately and investigate your claim.



A Novel Method to Derive Exospheric Temperatures from Swarm Thermospheric Densities during Quiet Times

Yingyun Lin ^{1,2} , Jiyao Xu ^{1,2,3,*}, Jose van den IJssel ⁴ and Wei Yuan ^{1,3}

¹ State Key Laboratory of Space Weather, National Space Science Center, Chinese Academy of Sciences, Beijing 100190, China

² University of Chinese Academy of Sciences, Beijing 100049, China

³ Hainan National Field Science Observation and Research Observatory for Space Weather, National Space Science Center, Chinese Academy of Sciences, Beijing 100190, China

⁴ Faculty of Aerospace Engineering, Delft University of Technology, 2629 HS Delft, The Netherlands

* Correspondence: jyxu@spaceweather.ac.cn; Tel.: +86-139-1102-8403

Abstract: One of the most important parameters in the atmosphere, the neutral temperature, becomes difficult to measure at high altitudes such as the exosphere. Therefore, based on the assumption of static equilibrium and isothermal atmosphere, a new method was developed to derive quiet-time exospheric temperatures using neutral atmospheric densities from 470 km to 550 km, which were obtained from the Swarm satellites. The derived neutral temperatures were obtained at an altitude of approximately 500 km in the low and middle latitudes from mid-April 2014 to early August 2014. The results were evaluated with nighttime temperatures from ground-based Fabry Perot Interferometers at 250 km. The mean deviation between the derived temperatures and FPI was 30.80 K and the standard deviation of the mean was 106.20 K. The diurnal variations of the exospheric temperatures, which tended to reach their maximum in the late afternoon, were in good consistency with the NRL-MSISE00 model simulations. This novel method performs well at low and middle latitudes. The greatest source of uncertainty is the mean molecular mass, which is also not well determined at these high altitudes. Hence, a measurement called “Satellite-tethered Mass Spectrometer Detection” was proposed to address this.

Keywords: exospheric temperature; static equilibrium; neutral density; scale height; Swarm



Citation: Lin, Y.; Xu, J.; van den IJssel, J.; Yuan, W. A Novel Method to Derive Exospheric Temperatures from Swarm Thermospheric Densities during Quiet Times. *Remote Sens.* **2022**, *14*, 5382. <https://doi.org/10.3390/rs14215382>

Academic Editor: Hanlim Lee

Received: 13 August 2022

Accepted: 24 October 2022

Published: 27 October 2022

Publisher's Note: MDPI stays neutral with regard to jurisdictional claims in published maps and institutional affiliations.



Copyright: © 2022 by the authors. Licensee MDPI, Basel, Switzerland. This article is an open access article distributed under the terms and conditions of the Creative Commons Attribution (CC BY) license (<https://creativecommons.org/licenses/by/4.0/>).

1. Introduction

Exospheric temperature is a fundamental physical quantity of the neutral atmosphere, and as such representing temperature and temperature variations in a realistic way is a key requirement for any model of the atmospheric state. To achieve this, observations are needed. However, the exospheric temperature is difficult to measure. The atmospheric density decreases with height, and the dominant neutral components become O, H, and He at higher altitudes, which increases the difficulty of detecting neutral atmospheric temperatures in the exosphere. Some methods used at lower altitudes, such as infrared detection using carbon dioxide and optical detection using airglow, are unsuitable for exospheric measurements. The ground-based Fabry Perot Interferometer (FPI) has become the predominant atmospheric detection equipment in the upper thermosphere, and there are few space-based approaches that exist for obtaining exospheric temperatures. However, FPI observations have limitations in local times, heights, and global distribution, because the number of FPI stations is limited and they only observe at a fixed altitude during nighttime.

Due to the lack of exospheric temperature observations, previous studies have presented a few methods to derive exospheric temperatures from other neutral parameters. For example, using the 300–500 km neutral density detected by the GRACE satellites, Burke determined a linear function of exospheric temperature with height and neutral density

and used this relationship in the Jacchia77 model [1]. Furthermore, based on the diffusion function of the Jacchia77 model and Burke's method, Wise used the neutral density from CHAMP/GRACE and performed temperature iteration to derive exospheric temperatures by forcing the model density to approximate the measured density [2]. Subsequently, he compared the derived temperatures with NRL-MSISE00 (MSIS) model [3] temperatures and exospheric temperatures from the HASDM model, which were all in good agreement. Additionally, Forbes used temperature iteration as well; he changed the input parameter F10.7 flux to ensure that the model density approximated the measured value from CHAMP/GRACE, which resulted in improved model exospheric temperatures [4]. Weimer also used the density from the CHAMP/GRACE observations, together with the MSIS model and a mapping method. They obtained exospheric temperatures and corrected them according to theoretical disturbances based on atmospheric formulas [5]. Weng et al. constructed an exospheric temperature model using the CHAMP density and the MSIS model [6]. The input parameters of Weng's model were latitude, longitude, local time, geomagnetic index, and F10.7 flux. They obtained temperatures from 2002 to 2020, which were well correlated with those from MSIS and GRACE. In addition, Evans used the N₂-LBH radiation band of the GOLD satellite, diffusion equilibria, and isothermal atmospheric theory to calculate exospheric temperatures by obtaining the integral of the volume emission rate along the line of sight using the Chapman function and the scale height of N₂ [7]. These attempts provide us with several applicable methods and new thinking about how to derive exospheric temperatures. Nevertheless, they have limits. For example, the methods of Burke, Wise, Forbes, and others depend strongly on model information and are therefore biased to the model results; while the method of Evans has fitting errors.

In view of the importance of a good knowledge of the neutral temperature at and above the thermosphere, and the difficulty to obtain good measurements, alternative methods to derive exospheric temperature are worth exploring. The previously mentioned methods obtain the exospheric temperature through other parameters. However, those methods are greatly depending on the model information. Hence, a new method was developed to derive exospheric temperatures from neutral densities at two different altitudes, to reduce the reliance on models. This method relies on the assumption that the atmosphere is at static equilibrium with isothermal conditions between the two altitudes. The exospheric temperatures at approximately 500 km were calculated using the neutral densities from the Swarm A/B/C satellites, which fly at two different altitudes separated by about 50 km. The derived temperatures are then compared with temperatures from ground-based FPI and model simulations. However, the role of mean molecular mass cannot be ignored in the inversion. There is a large dispersion of mean molecular mass both in temporal and spatial distribution. Assuming a mean molecular mass of 16 and a temperature of 1000 K, a small change of only 0.1 in mean molecular mass results in a temperature change of 7 K, which shows that the mean molecular mass has to be carefully selected. In this work, MSIS model simulations are used to obtain the mean molecular mass, but this might introduce errors, due to the model uncertainties. Therefore, to solve this problem, a detection method called "Satellite tethered Mass Spectrometer Detection" was proposed to obtain densities of specific components in order to determine the mean molecular mass.

Section 2 describes the data, model and method, and also provides an error estimate of the method. Section 3 details the comparisons between the derived temperatures, the ground-based FPI temperatures, and MSIS model simulations to evaluate this method. Section 4 proposes the detection idea, its estimation of the design, and the error evaluation. Finally, Section 5 summarizes this work.

2. Data and Methods

2.1. Data and Model

2.1.1. Swarm Satellites

The Swarm [8] satellites were launched on 22 November 2013, and are still operating today. These three satellites, named Swarm A, Swarm B, and Swarm C, have similar

original weights, volumes, and 510 km orbiting heights. Due to the limited availability of accelerometer-derived densities due to accelerometer instrument issues, we use the derived neutral mass densities [9,10] from GPS precision orbit determination data instead in this study. The temporal and spatial resolution of the data points of the GPS-derived densities are 30 s in time, and 2.2° in latitude. However, the 30 s sampling does not reflect the actual signal information of the relatively smooth densities. High-frequency signals are not well recovered and therefore the temporal resolution of the GPS-derived density signal is about 20 min. Since the Swarm satellites are in near-polar orbits, at middle and low latitudes, the satellite tracks have small variations in longitude; at high latitudes, this varies much more rapidly. The daily average altitudes and neutral densities of the Swarm satellites during 2013–2020 are provided in Figure 1. This shows that the satellites were flying closely together initially. Two months later, they separated and were maneuvered to their selected orbits until 15 April 2014. After this, Swarm A and C flew together at an altitude of approximately 462 km with a 1.4° longitude interval; Swarm B was flying at a higher altitude of approximately 511 km. The satellites have gradually declined in orbit over time. In this study, the data range we used is from 15 April 2014 to 11 August 2014. During this period, the relative errors of the GPS-derived densities for the high-flying and lower-flying satellites are estimated to be, respectively 7% and 4% [10].

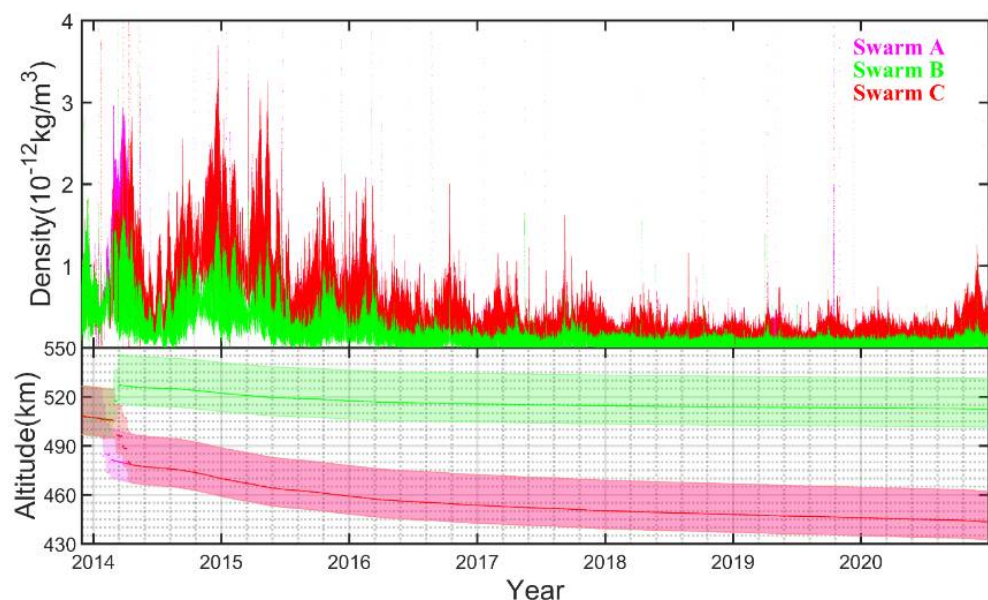


Figure 1. Daily mean altitudes and neutral densities of the Swarm satellites (The colors of Swarm A, Swarm B, Swarm C are pink, green and red. The densities of Swarm A and Swarm C overlap because the two satellites are flying closely together).

2.1.2. The Ground-Based Fabry-Perot Interferometer

The Fabry-Perot Interferometer is a multi-beam Interferometer [11,12] that uses the principle of Doppler interference to derive temperature through observed interference fringes. As the light of these airglows is weaker than the sunlight, it is difficult to observe during the daytime. Nighttime ground-based FPI temperatures are, however, reliable, and widely used in thermospheric research. There are many emission bands for FPI, which are located at different altitudes. In this work, the airglow data in the O630.0 nm band was used, because only the detection altitude of this band can reach the thermospheric altitude. The emissions of O630.0 nm are integrated from 200 km to 300 km to derive temperatures, and because the emission of O630.0 nm airglow reaches its maximum at the altitude of 250 km, it is generally considered that the altitude of the detection data is 250 km. We use the measured FPI temperatures at 250 km to evaluate the derived results at 500 km. According to the atmospheric profile provided by MSIS in Figure 2, temperature increases

strongly with altitude until a certain altitude, after which this levels off until the variations in temperature become very small. According to MSIS, this altitude was just below 250 km in 2014; hence, the deviations in temperatures between 250 km and 500 km are considered relatively small when compared to the background temperatures.

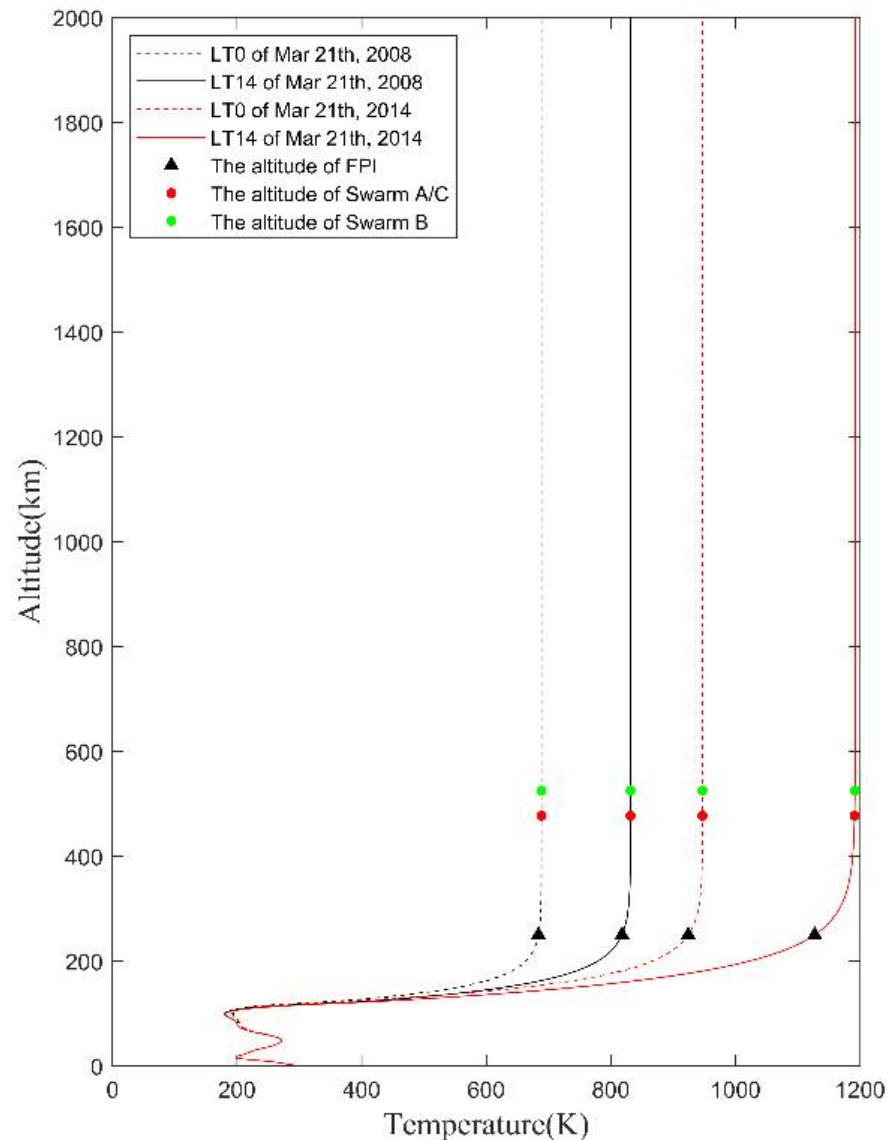


Figure 2. Variation of daytime and nighttime neutral temperatures with altitudes in 2008 and 2014. The green dots are the temperature of Swarm B, the red dots are the temperature of Swarm A and Swarm C, the black triangles are the temperatures at FPIs' altitude.

Table 1 shows the geographical locations of FPIs, and the number of data points used in the comparison. In the comparison between FPI and derived temperature results, the nighttime temperatures from seven ground-based FPI stations in 2014 were used, consisting of the Xinglong station of the Meridian Program in Hebei, China, and six stations of the Madrigal Database, such as Millstone Hill station. FPI observations are strongly affected by the weather and other environmental conditions and become unreliable when it's rainy or foggy. In such weather, it is difficult to observe the airglow emission clearly. The Madrigal data have a validity indicator, when validity 0 means the quality of the data is good, validity 1 means the data needs to be considered, and validity 2 means the quality of the data is bad. Unreliable data were removed using the data validity indicator from the Madrigal

Database and using the FPI cloud map for the Xinglong station. Only the data with validity 0 or 1 from Madrigal and sunny days from Xinglong were used in this work.

Table 1. Geographical locations of FPI stations and their number of selected observations. Positive latitude and longitude represent north and east.

FPI Station	Latitude	Longitude	Used Observations in the Comparison
Arecibo	18.34°	−66.75°	14
Pisgah	35.2°	−82.85°	41
Virginia	37.2°	−80.42°	52
Eastern Kentucky	37.75°	−84.29°	27
Urbana	40.13°	−88.2°	38
Xinglong	40.2°	117.4°	27
Peach mountain	42.27°	−83.75°	4

2.1.3. NRL-MSISE00 Model

NRL-MSISE00(MSIS) [3] is an empirical model of the neutral atmosphere. The model is based on fundamental equations and observations from non-coherent scatter radars and satellites. It can provide global temperature, density, and number density of different atmosphere components from ground to 2000 km altitude. The input parameters of MSIS are the day of the year, UT, latitude, longitude, f10.7 flux, and geomagnetic Ap index, and the output are neutral atmospheric temperature, atmospheric mass density, and number density of O, O₂, N₂, H, H₂, N, Ar.

2.2. New Method for Temperature Calculation

Thermospheric density ρ varies with height, as follows:

$$\rho(z) = \rho_0 e^{-\frac{z}{H(z)}}, \quad (1)$$

$$H(z) = \frac{RT_v(z)}{\bar{m}(z)g(z)} \quad (2)$$

where z is the altitude, H is the scale height, T_v is the atmospheric temperature, \bar{m} is the mean molecular mass, R is the gas constant, and g is the gravitational acceleration.

The gravitational acceleration g at high altitude was calculated as follows:

$$g(r) = \frac{GM}{r^2} \quad (3)$$

where G is the gravitational constant, M is the mass of the Earth, and r is the distance from the core of the Earth to the target point.

We assume the atmosphere is in static equilibrium, so the scale heights and temperatures are constant in the area between the two Swarm satellites. When substituting ρ_1 and ρ_0 for the densities of the higher and lower flying satellites, Equation (1) becomes:

$$\rho_1 = \rho_0 e^{-\frac{h_1 - h_0}{H}} \quad (4)$$

We used the average of the mean molecular mass and the gravity acceleration of the upper-flying satellite and lower-flying satellites as regional approximations in the calculations, and combined with Equation (2), the temperature in this region was determined by:

$$T_v = \frac{H\bar{m}g}{R} = \frac{-(h_1 - h_0) \cdot \bar{m}g}{\ln\left(\frac{\rho_1}{\rho_0}\right) \cdot R} \quad (5)$$

Because in-situ observations of the mean molecular mass are unavailable for the Swarm satellites, we used two different approaches to derive mean molecular mass:(1) Based on

Equation (5), the mean molecular mass can be obtained from the known temperatures and densities at two different altitudes, so we simulated the temperatures and densities of Swarm A/C and Swarm B using MSIS, and thus derived the corresponding mean molecular mass \bar{m}_s along the Swarm orbits; (2) We calculated the global mean molecular masses in 2014 using the number densities of different atmospheric components from MSIS. The selected time period was from April 2014 to June 2014, which is comparable with the time period of the FPI observations, and the latitude and longitude ranges were from -60° to 60° geomagnetic latitude, 0° – 360° geomagnetic longitude, 5° , and 10° grids, respectively. We averaged all the values of mean molecular mass to obtain a constant $\bar{m}_0 = 16.0318$ with a standard deviation of 1.2%. It should be noted that the constant \bar{m}_0 approach was used in order to further reduce the dependence on the MSIS model input.

In both cases, the gravitational acceleration was computed along the Swarm orbit using the average altitude of the upper-flying and lower-flying satellites.

To find conjunctions between Swarm B and the lower satellite pair, a single-point sliding window was used. The window was centered on Swarm B, with a latitudinal width of $\pm 2.5^\circ$, a longitudinal width of $\pm 7.5^\circ$, and a time range of ± 5.5 min. When Swarm A or Swarm C entered the window, they were regarded as having the same observation conditions as Swarm B.

Using the sliding window mentioned above, we obtained 81011 points of temperature from 2014 to 2020 at an altitude of approximately 500 km. Due to complex disturbances and a lack of FPI observations in the high latitudes and polar regions, only the temperatures at the low and middle latitudes were considered, which are shown in Figure 3. Low latitude conjunctions between the higher-flying satellite and the lower pair only occurred from mid-April to early August in 2014; they otherwise occurred in the polar regions. Due to the orbit plane configuration of Swarm during this time span, a period of up to 19 h of low latitude conjunctions occurred every 6 days. Therefore, the inversion results were obtained every sixth day from mid-April to early August in 2014, and the frequency of occurrence of the derived results is half an hour during the 19 h of the conjunction. In the following section, the data for these three months are further analyzed.

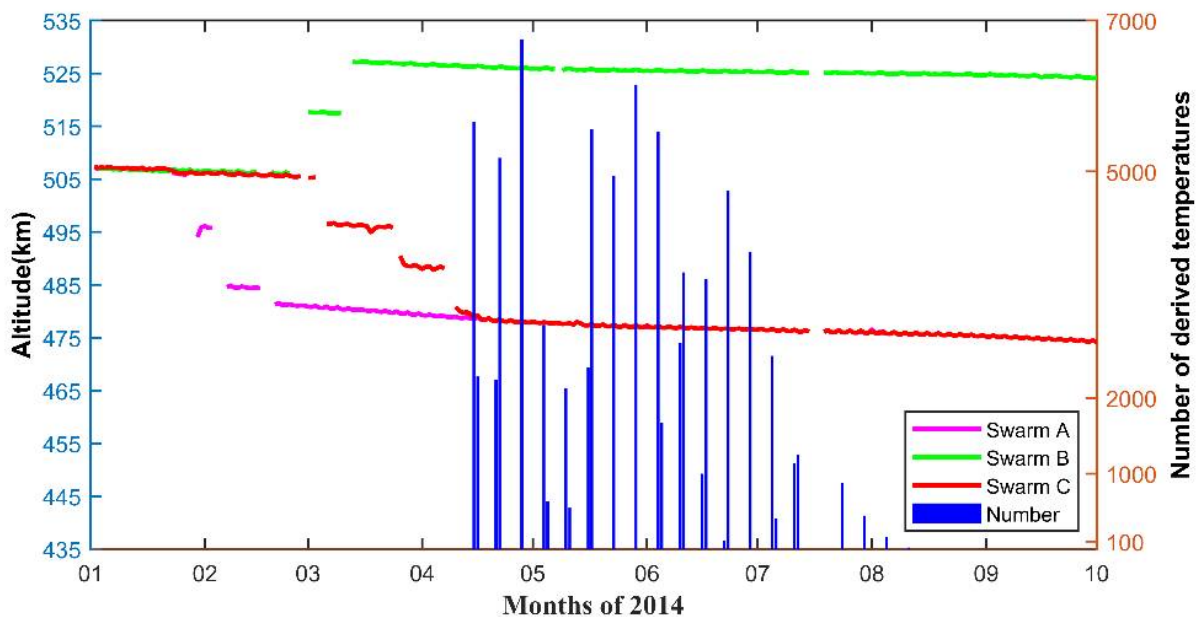


Figure 3. Time distribution of inversion temperatures from January 2014 to October 2014, the result number is the number of points in the low and middle latitudes.

2.3. Sources of Uncertainty

If $(\frac{\rho_1}{\rho_0})$ is set to x , the Taylor expansion of Equation (5) is given as

$$T = T_0 + \frac{-\Delta z \cdot m \cdot g}{\ln^2(x) \cdot R} \cdot \frac{1}{x} \cdot \Delta x + \frac{-\Delta z \cdot g}{\ln(x) \cdot R} \cdot \Delta m + \frac{-\Delta z \cdot m}{\ln(x) \cdot R} \cdot \Delta g, \quad (6)$$

Thus, the relative error of this method can be expressed as

$$\frac{\Delta T}{T} = \frac{1}{\ln(x)} \frac{\Delta x}{x} + \frac{\Delta m}{m} + \frac{\Delta g}{g} \quad (7)$$

Equation (7) shows that the relative error consists of three parts, the measurement error of the Swarm densities, the error of the mean molecular mass, and the error of gravitational acceleration. For the Swarm densities in 2014, the relative error is estimated to be about 7% and 4% for, respectively, Swarm B and the lower pair. The mean value of the relative error of $(\frac{\rho_1}{\rho_0})$ is then about $3.01\% \pm 11.015\%$, and $\frac{1}{\ln(x)}$ becomes 1.30.

The mean molecular mass is obtained using MSIS model information. MSIS is a climatological empirical atmospheric model, and it shows a good long-term variation of atmospheric temperatures and neutral compositions. However, there are deviations between the MSIS model and the actual atmosphere and this introduces uncertainties. It is difficult to determine the uncertainty of the modeled mean molecular mass, because there are no actual data for comparison. The error of the mean molecular mass due to the regional approximation, which is a result of the averaging between altitudes, can be estimated. To access this, the global mean molecular masses at the average altitudes of upper-flying and lower-flying satellites (about 477 km and 525 km) are obtained from MSIS similar to (1) in Section 2.2. The deviations between the nominal mean molecular masses and the global mean values at these two altitudes can be used to determine the relative error of the mean molecular mass, which is $3.25\% \pm 9.89\%$. In the same way, the gravitational acceleration at the average altitudes of the upper-flying and lower-flying satellites are determined, which leads to a relative error of gravitational acceleration of 0.7%. Substituting these three errors into Equation (7), the total relative error of this method becomes $7.86\% \pm 17.4\%$.

3. Temperature Comparisons between Observations, Model Simulations, and Inversion Temperatures

The derived temperatures from 15 April 2014 to 11 August 2014 were used for analysis, and their variations in latitude and local time are shown in Figure 3. It should be noted that temperature data are not available every day, but at a frequency of every 6 days, so there are only 30 days of data in this period. The results cover $0^\circ - 360^\circ$ in longitudes and -60° to 60° in latitude and do not cover 24 h completely. Figure 4 shows there is a lack of temperatures in LT 2:00–6:00 and LT 14:00–16:00. In this section, we evaluate the derived temperatures using statistical deviations and diurnal variation characteristics. For brevity of the text, we refer to the derived temperatures calculated with \bar{m}_s by $T(\bar{m}_s)$, the derived temperatures calculated with \bar{m}_0 by $T(\bar{m}_0)$, the temperatures of FPI by $T(FPI)$ and the temperatures of MSIS by $T(MSIS)$.

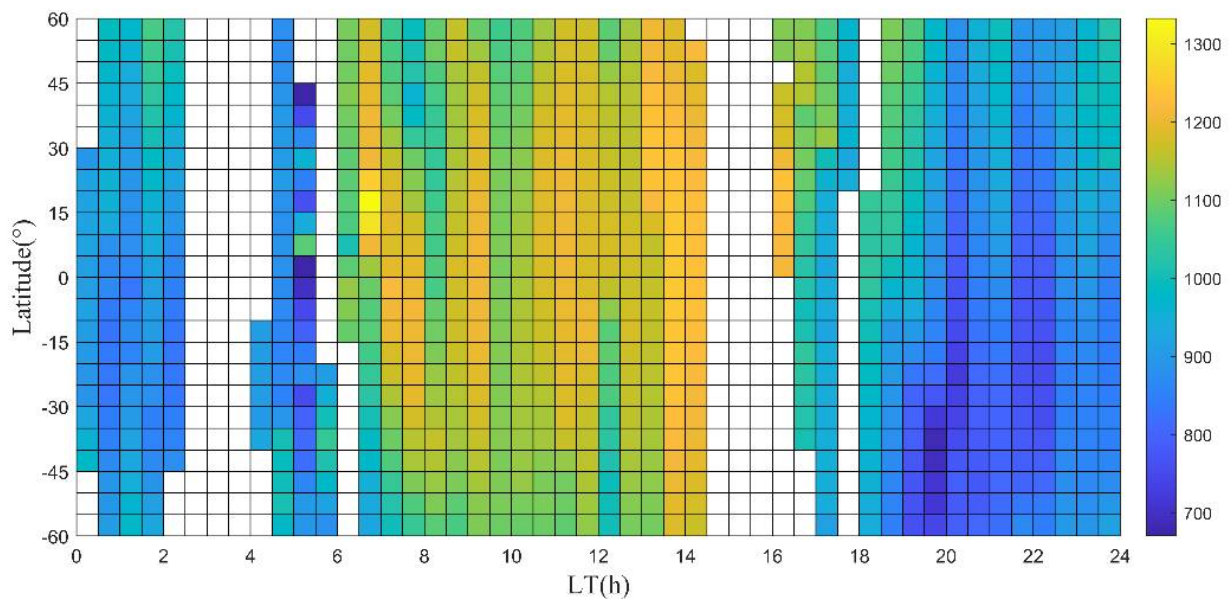


Figure 4. The diurnal variation of derived temperatures (K) from 15 April 2014 to 11 August 2014.

3.1. Quantitative Comparison between Derived Temperatures, Ground-Based FPI Measured Temperatures and MSIS Simulations

Since there were no derived temperatures at the exact locations of the FPI stations, a window was again used to obtain conjunctions. The window was centered on the locations of the FPIs, with latitudinal and longitudinal widths of $\pm 2.5^\circ$ and $\pm 7.5^\circ$, respectively. If the derived temperatures were located inside the window, they were considered to be under the same observation conditions. Additionally, cubic-spline interpolation was used to obtain the FPI temperatures at the same time as the derived temperatures. To minimize interpolation errors, a relatively small two-hour range was selected to fit a smooth trend. In addition, since the atmospheric conditions during the disturbance period do not support our assumption, those data points with $K_p > 2$ or $Dst \leq -30$ are discarded. It should be noted that the effect of geomagnetic disturbances on neutral density can last for a few hours [13,14], therefore, ideally the geomagnetic indexes of both the current day and the previous day need to be considered. However, in this case, the remaining data are not enough for subsequent analysis. Therefore, only the geomagnetic index of the current day was considered. In this way, 203 data points were obtained for comparison (see Appendix A), and they were all at nighttime.

For the comparison between the derived temperatures and the MSIS comparison, MSIS model temperatures were determined corresponding to each derived temperature. In this case, the whole database of 81011 points is used for the comparison, including daytime and nighttime data.

The comparison was evaluated by the mean deviation and the standard deviation of the mean. First, a point-to-point deviation of the derived temperatures, FPI temperatures, and MSIS temperatures was obtained; from these differences, the mean deviations and the standard deviations of the mean were calculated. Table 2 shows the results of the statistical analysis of the derived temperatures calculated with different mean molecular masses compared with FPI and MSIS temperatures, respectively.

The comparison results of the derived temperatures and the FPI temperatures are analyzed first. As shown in Appendix A, the range of derived temperatures and the FPI temperatures was in both cases between 850 K to 1100 K. Table 2 shows that the mean deviation between $T(\bar{m}_s)$ and $T(FPI)$ is 30.80 K, indicating that $T(\bar{m}_s)$ was larger than $T(FPI)$ in general. According to MSIS, the expected temperature deviations between 250 km and 500 km are small. The mean temperature deviation between 250 km and 500 km simulated by MSIS is 23.52 K, which is close to the mean deviation between $T(\bar{m}_s)$

and $T(FPI)$. However, the standard deviation between $T(\bar{m}_s)$ and $T(FPI)$ is 106.20 K, while that of MSIS is 14.53 K. Such a large great difference is probably due to the fact that temperature variations in MSIS simulations are much smaller than the variations in the actual atmosphere. The differences between $T(\bar{m}_s)$ and $T(FPI)$ are considered to be caused both by the temperature deviation between 250 km and 500 km altitude and the uncertainties of our method, which were estimated in Section 2.3.

The expected error of the method can be determined, as explained in Section 2.3. Using the average temperature of the samples in Table 2, the error is $73.98 \text{ K} \pm 179.78 \text{ K}$. The deviation between $T(\bar{m}_s)$ and $T(FPI)$ is $30.80 \text{ K} \pm 106.20 \text{ K}$, which is smaller than the estimated method error.

The negative mean deviation between $T(\bar{m}_0)$ and $T(FPI)$ indicates that the derived temperatures are lower, which does not conform to the theoretical relation that the temperature at 500 km is larger than at 250 km. The standard deviation between $T(\bar{m}_s)$ and $T(FPI)$ is 108.03 K, which is close to that between $T(\bar{m}_s)$ and $T(FPI)$, but slightly larger. From these results, we conclude that the use of the constant \bar{m}_0 increases the bias. It is shown that the mean molecular masses have a great influence on the derived temperature, and more reliable results are obtained with \bar{m}_s .

Table 2. Comparative statistical analysis of inversion temperatures calculated with \bar{m}_0 and \bar{m}_s , FPI temperatures and MSIS simulations.

Temperatures for Comparison	Sample Points	Mean Deviation, K	Standard Deviation, K
$T(\bar{m}_s)$ & $T(FPI)$	203	30.80	106.20
$T(\bar{m}_0)$ & $T(FPI)$	203	−30.67	108.03
$T(\text{MSIS at 500 km})$ & $T(\text{MSIS at 250 km})$	203	23.52	14.53
$T(\bar{m}_s)$ & $T(\text{MSIS})$	81011	16.52	84.46
$T(\bar{m}_0)$ & $T(\text{MSIS})$	81011	45.90	140.73

Moreover, the last two rows of Table 2 show that the mean deviation between $T(\bar{m}_s)$ and $T(\text{MSIS})$ is $16.52 \text{ K} \pm 84.46 \text{ K}$, while the mean deviation between $T(\bar{m}_0)$ and $T(\text{MSIS})$ is $45.90 \text{ K} \pm 140.73 \text{ K}$. The better agreement between $T(\bar{m}_s)$ and $T(\text{MSIS})$, compared to $T(\bar{m}_0)$, also supports the use of \bar{m}_s .

3.2. Comparison between Inversion Temperatures Calculated with \bar{m}_s , Ground-Based FPI Measured Temperatures and MSIS Simulations

The derived temperatures can also be evaluated by analyzing the diurnal variations of FPI temperatures, MSIS simulations, and derived temperatures at different latitudes. It should be noted that because the neutral temperature is sensitive to solar radiation, there are different variation characteristics in different months. Unfortunately, there are not enough data to show a complete diurnal variation per month, so all the data from April to August were put together to obtain an almost 24-h LT coverage. Due to this, our results are expected to be slightly different when compared to MSIS, and therefore only the general trends are analyzed in this evaluation.

Based on the distribution of temperatures in latitudes, the results were divided into 8 latitudinal bands, with about 10,000 points per latitude band. In order to get clear variation trends, the temperatures were averaged every 0.5 h from LT0–LT24 in each latitudinal band and plotted with an error bar. Figures 5 and 6 show the diurnal variations in temperatures of MSIS, FPI, and derived temperatures calculated with \bar{m}_s and \bar{m}_0 , where the horizontal axis is local time, and the vertical axis is temperature. The black dots indicate the derived temperatures, the red dots are the MSIS simulated temperatures, the red smoothed curves are the variation trends fitted with red dots, and the black triangles are the FPI observations.

Figure 5 shows that during the daytime, the diurnal trends of the derived temperature are greatly consistent with the point-by-point MSIS simulations at latitudes except for

LT8–LT9. At night, in the northern hemisphere, the derived temperatures in the first half of the night at low latitudes are generally lower than those obtained with MSIS simulations, and in the second half of the night, they are generally higher. At middle latitudes, they are higher than the MSIS temperatures. On other hand, in the southern hemisphere, the derived temperatures are smaller than the MSIS simulations in both the first and second half of the night. In addition, though the FPI observations are mainly distributed in the 30°N–45°N latitude zone, the derived temperatures in this zone also show a similar nighttime variation trend.

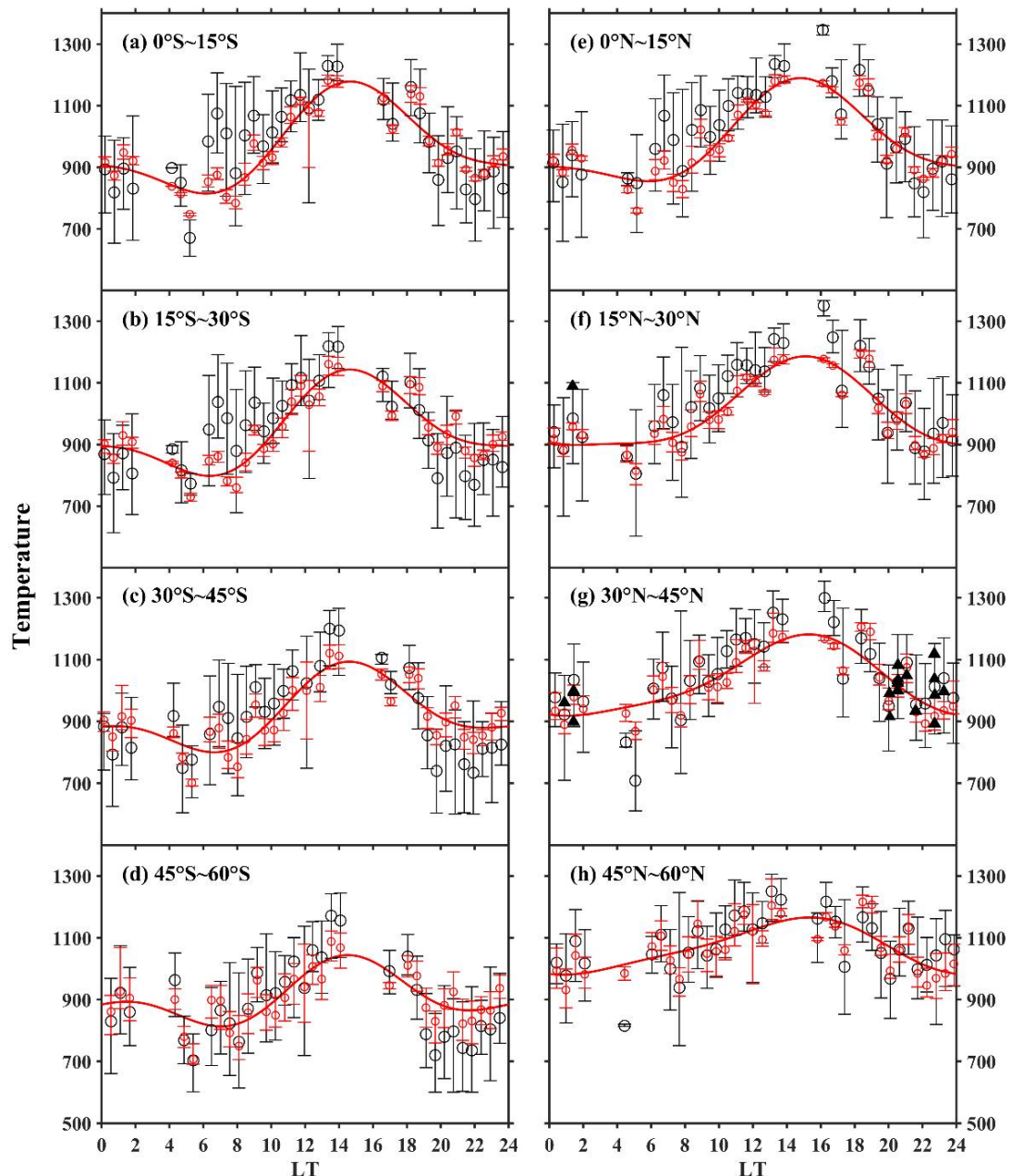


Figure 5. Diurnal variation of derived temperatures calculated with \bar{m}_s , model temperatures and ground-based FPI temperatures. The duration is from mid-April to early August in 2014. Black dots represent the derived temperatures, red dots represent the MSIS temperatures, red line represents the fitted curve of red dots; and black solid triangles represent the ground-based FPI temperatures during this time. The left side represents the four latitude bands of the Southern Hemisphere, and the right represents the Northern Hemisphere.

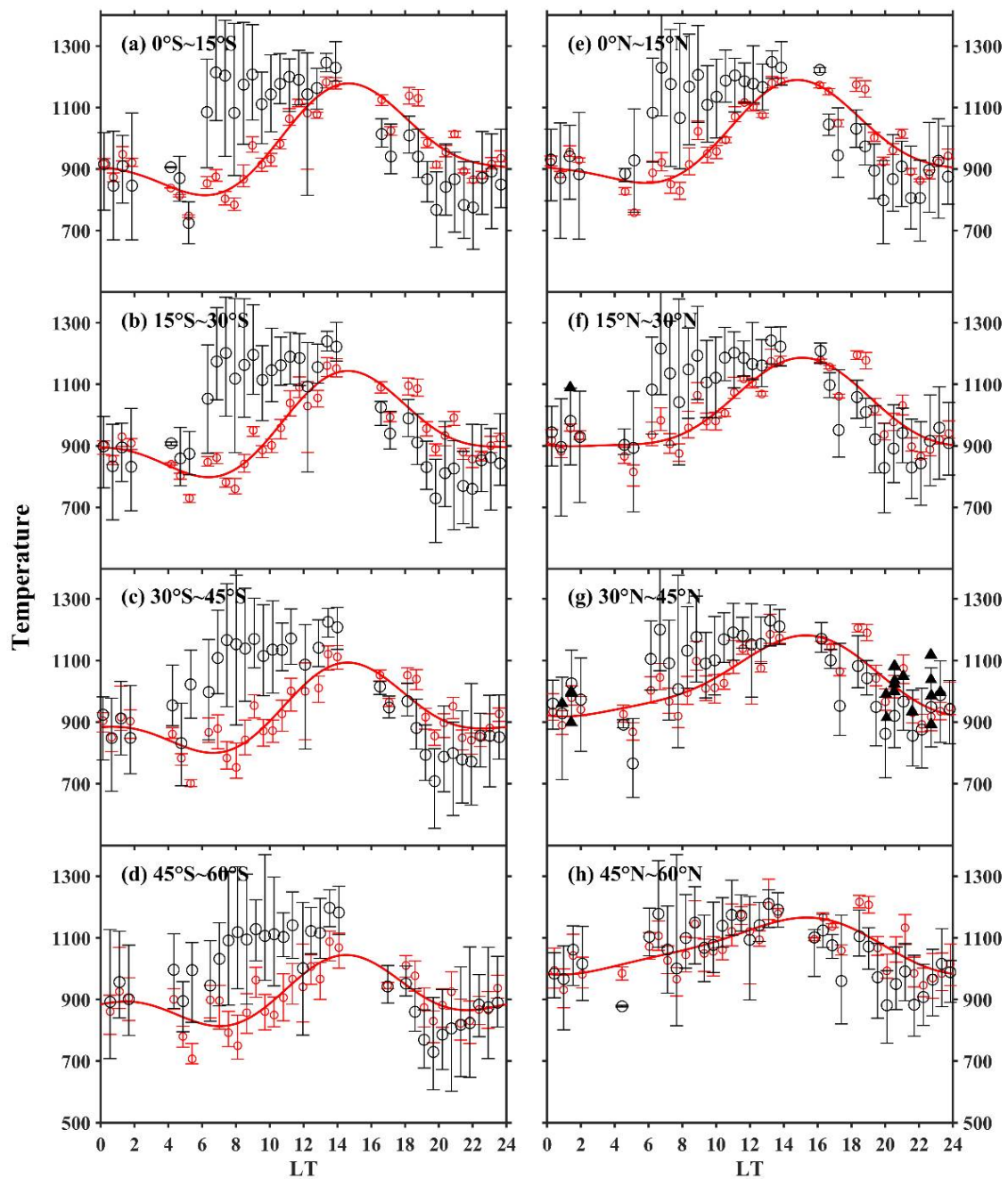


Figure 6. Diurnal variation of derived temperatures calculated with \bar{m}_0 , model temperatures and ground-based FPI temperatures. The duration is from mid-April to early August in 2014. Black dots represent the derived temperatures, red dots represent the MSIS temperatures, red line represents the fitted curve of red dots; and black solid triangles represent the ground-based FPI temperatures during this time. The left side represents the four latitude bands of the Southern Hemisphere, and the right represents the Northern Hemisphere.

The enhancement of LT8–LT9 shown in Figure 5 is stronger at low latitudes than at middle latitudes, and stronger in the southern hemisphere than in the northern hemisphere. Based on earlier findings, the same enhancement of LT8–LT9 was observed by the incoherent scattering radar [15] in Millstone Hill which is located at 42°N. These observations show the relation between enhancement and solar activities. At present, however, there are not enough data to further analyze this.

In Figure 6, $T(\bar{m}_0)$ also showed diurnal variation, as well as similar nighttime characteristics as $T(\bar{m}_s)$ in Figure 4. However, in the daytime, the derived temperatures are very different from the MSIS simulations, especially in the southern hemisphere. This might be caused by the use of mean molecular mass \bar{m}_0 . \bar{m}_0 was calculated with the mean molecular masses in the spring and summer of the northern hemisphere and in the autumn and winter of the southern hemisphere. The resulting average \bar{m}_0 is then much larger than the value for the southern hemisphere.

In general, the derived temperatures all have diurnal trends and reach their maximum in the afternoon (around LT14). As there was no data in LT2–LT6, and the theoretical minimum usually occurs during this period, the minimum of the diurnal variation was not analyzed. The trends of $T(\bar{m}_s)$ and $T(\bar{m}_0)$ are very different during the day. In general, $T(\bar{m}_s)$ is greatly consistent with MSIS simulations but differs in some details. This indicates that $T(\bar{m}_s)$ performs qualitatively well, while $T(\bar{m}_0)$ shows more obvious problems.

The two derived temperatures vary considerably due to the difference between the mean molecular mass. Figure 7 shows the diurnal variation of \bar{m}_s . It can be found that \bar{m}_s reaches its maximum around LT18 and its minimum around LT8. Moreover, the difference of \bar{m}_s between the northern and southern hemispheres is considerable, with lower \bar{m}_s in the southern hemisphere. Figure 7 shows that the center of the maximum is in the northern hemisphere and the center of the minimum is in the southern hemisphere. Comparing Figures 5 and 6, the difference between the two derived temperatures is mainly in the local time from morning to before noon, during which the value of $T(\bar{m}_0)$ is larger than that of $T(\bar{m}_s)$. According to Figure 7, the difference is obviously caused by the variation of mean molecular mass. Thus, it should be noted that the mean molecular mass plays an important role in the inversion, and its variation with time and location is not negligible.

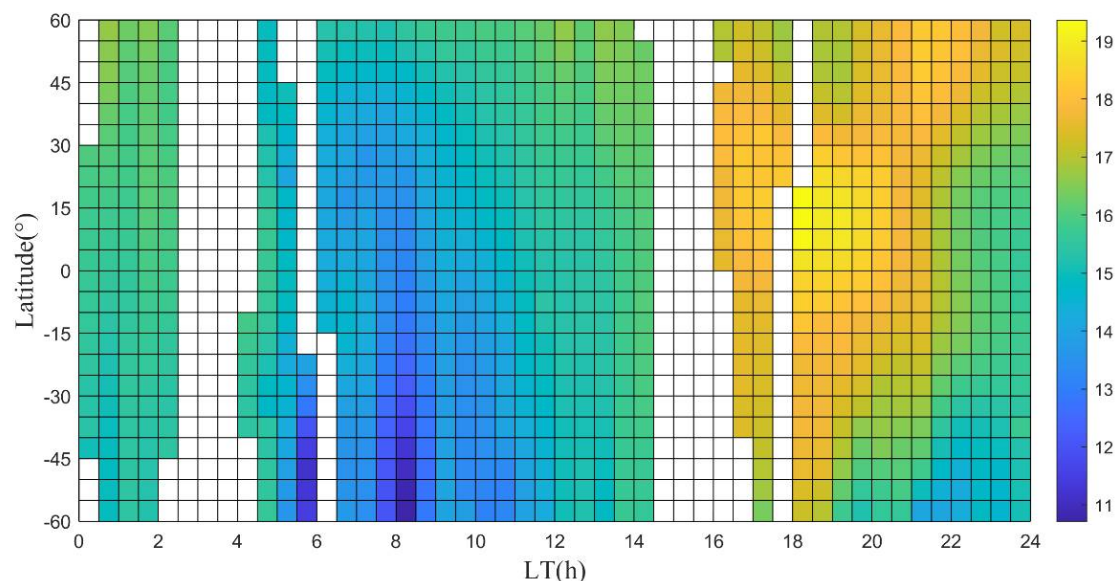


Figure 7. The diurnal variation of mean molecular mass \bar{m}_s (g/mol) from 15 April 2014 to 11 August 2014 (The same calculation as Figure 4).

4. A New Concept “Satellite-Tethered Mass Spectrometer Detection”

Information on the mean molecular mass is required for our method to derive temperatures. Since in situ observations are not available, we had to use MSIS simulations. In order to reduce the model dependency, a constant mean molecular mass was also used to derive temperatures. However, this value causes a large deviation in the obtained results. To determine the mean molecular mass, a detection idea, “Satellite-tethered Mass Spectrometer Detection”, is proposed. Its schematic is shown in Figure 8.

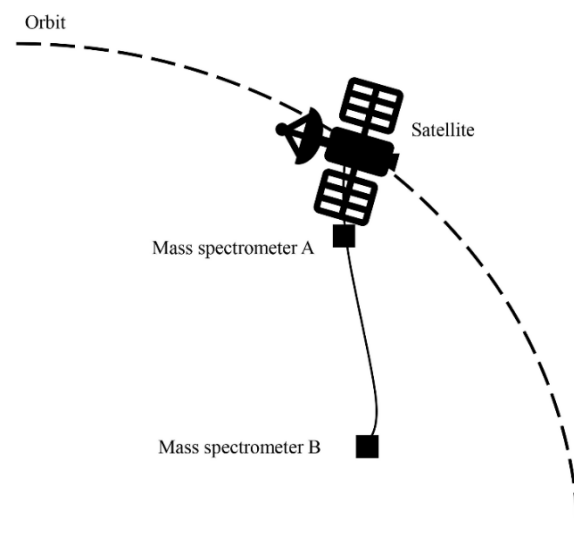


Figure 8. The schematic diagram of Satellite tethered Mass Spectrometer Detection.

The concept consists of one satellite that carries two independent mass spectrometers that are separated by a certain distance and are used to detect the density at two different altitudes for multiple atmospheric components, such as O, H, etc. From these observations, the mean molecular mass can be determined, and combined with Equation (5) in Section 2.2, the neutral temperature of these different components can be derived.

Figure 9 shows the relationship between the estimation error, the wire length, and the densities measurement errors. The error estimation is based on Equation (7), and the influence of both the wire length, varying between 1–50 km, and a relative density measurement error in the 1–20% range on the total error were investigated. If the total error should be limited to 10%, and if the measurement error of the mass spectrometers is set to be 3%, under the worsts estimation (the relative error of $(\frac{\rho_1}{\rho_0})$ reaches its maximum), the relative error of densities could reach 6%. In this case, the wire length should be at least 15 km. This is a preliminary estimation, and the wire length should be reconsidered according to the actual situation and the requirements for the total error. With this detection method, there is no need to use a model to simulate the mean molecular mass. Possibly, some extra observations can also be obtained, such as the neutral temperatures of different components.

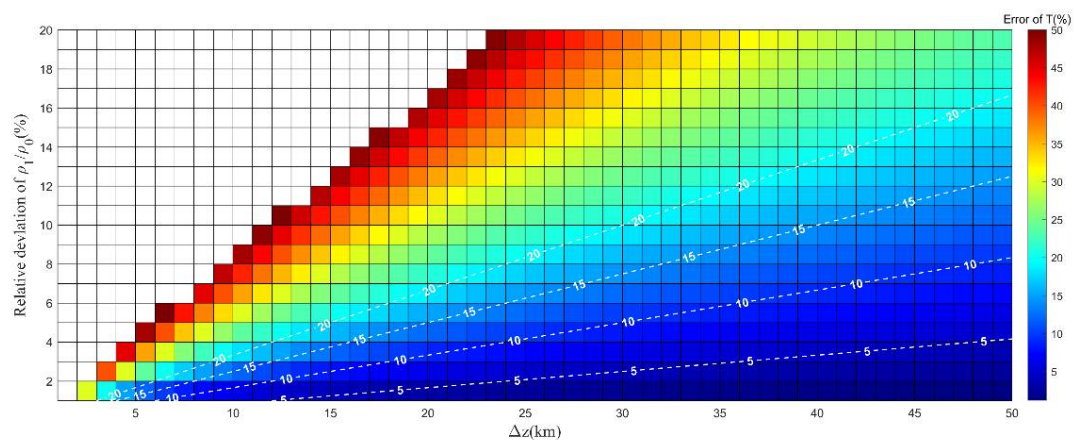


Figure 9. The relationship between the relative errors, wire length and densities' measurement error. The horizontal axis indicates the wire length, the vertical axis indicates the relative error of $(\frac{\rho_1}{\rho_0})$, and the color indicates the error of the derived temperatures. The dashed line shows the different error of derived temperatures.

5. Conclusions

The exospheric temperature is an important parameter, which is difficult to obtain. Therefore, a new method was developed to derive exospheric temperatures using densities at two different altitudes from the Swarm satellites, which reduces the reliance on the model information. Based on the assumption of atmospheric static equilibrium and an isothermal atmosphere, 81,011 points of neutral temperatures from mid-April 2014 to early August 2014 were obtained. These temperatures were mainly distributed at low and middle latitudes, at altitudes of around 500 km. By comparing with ground-based FPIs' nighttime temperatures at 250 km and corresponding NRL-MSISE00 model temperatures, the derived results were evaluated, and the following conclusions were drawn:

(1) The derived temperatures and FPI temperatures both lie between 850 K to 1100 K at nighttime. The deviation between the derived temperatures calculated with \bar{m}_s and FPI is $30.80 \text{ K} \pm 106.20 \text{ K}$. The deviation between the derived temperatures calculated with \bar{m}_0 and FPI is $-30.67 \text{ K} \pm 108.03 \text{ K}$. We also simulated the temperatures deviation between 250 km and 500 km by MSIS, the deviation is $23.52 \text{ K} \pm 14.53 \text{ K}$. The mean deviation between $T(\bar{m}_s)$ and $T(FPI)$ is close to the expected deviation between 250 km and 500 km obtained by the MSIS model, while the deviation between $T(\bar{m}_0)$ and $T(FPI)$ is larger. This indicates that $T(\bar{m}_s)$ is more reliable. Moreover, the deviation between $T(\bar{m}_s)$ and $T(MSIS)$ is $16.52 \text{ K} \pm 84.46 \text{ K}$; while the deviation between $T(\bar{m}_0)$ and $T(MSIS)$ is $45.90 \text{ K} \pm 140.73 \text{ K}$. This shows that $T(\bar{m}_s)$ agrees better with MSIS.

(2) The diurnal temperature trends from April to August 2014 were used to evaluate the derived results. The diurnal variation trends show that both $T(\bar{m}_s)$ and $T(\bar{m}_0)$ reach a maximum in the late afternoon. The diurnal variation trends of $T(\bar{m}_s)$ are greatly consistent with MSIS, with few differences in details. A noticeable difference is the temperature enhancement present in $T(\bar{m}_s)$ at LT8–LT9; moreover, the $T(\bar{m}_s)$ is slightly smaller than MSIS in the nighttime before midnight and slightly larger than MSIS in the nighttime after midnight at low latitudes in the Northern hemisphere. At middle latitudes, in the Northern hemisphere, $T(\bar{m}_s)$ is higher than MSIS at nighttime. However, in the Southern Hemisphere, it is lower than MSIS at nighttime. Moreover, in the band of 30°N–45°N, the derived temperatures and FPI temperatures also have similar variation trends at nighttime. In addition, $T(\bar{m}_0)$ differs significantly from MSIS during the daytime in the Northern Hemisphere and throughout the Southern Hemisphere.

(3) The mean molecular mass has a great influence on the derived temperatures. As this information is difficult to obtain from observations, it is the largest source of uncertainty in the method. In order to improve this and obtain more accurate exospheric temperatures, a measurement concept called "Satellite-tethered Mass Spectrometer Detection" was proposed. It detects the number densities of different atmospheric components like O, H, He et al. through a satellite carrying two mass spectrometers at a certain separational distance, and uses this information to derive exospheric temperatures. This detection does not need to use the simulations of the mean molecular mass in the calculation, also can obtain the exospheric temperatures of different atmospheric components, and therefore can be used to improve atmospheric empirical models.

The exospheric temperature retrieval method performs well in low and middle latitudes during quiet times. However, for polar regions and disturbance periods, there are currently not sufficient data for analysis. The orbits of the Swarm constellation change over time, and a period of regular low latitude conjunctions between Swarm B and the lower pair was again obtained during the summer of 2021. Further studies can be performed when more conjunction data become available.

Author Contributions: J.X.: Conceptualization, methodology; Y.L.: calculation, formal analysis, writing—original draft preparation; W.Y.: inversion FPI temperature data provision; J.v.d.I.: inversion Swarm neutral density provision, writing—review and editing. All authors have read and agreed to the published version of the manuscript.

Funding: This work was supported by the National Natural Science Foundation of China (41831073, and 42174196), the Chinese Meridian Project, and the Specialized Research Fund for State Key Laboratories, the Project of Stable Support for Youth Team in Basic Research Field, CAS (YSBR-018) and the National Key R&D program of China (2021YFE0110200), the International Partnership Program of Chinese Academy of Sciences. Grant No. 183311KYSB20200003.

Data Availability Statement: Publicly available datasets were analyzed in this study. They can be found here: the thermospheric neutral density data of Swarm satellites are available online (https://swarm-diss.eo.esa.int/#swarm%2FLevel2daily%2FLatest_baselines%2FDNS%2FFOD); the global atmospheric model NRL-MSISE00 can be obtained online (through the website <https://ccmc.gsfc.nasa.gov/pub/modelweb/atmospheric/msis/nrlmsise00/>). [Dataset] National Space Science Center, Chinese Academy of Sciences. 2010-06-25. Inversion data from FPI at Xinglong station. National Space Science Data Center. V1.0. DOI:10.12176/01.05.009.

Acknowledgments: We thank the Chinese Meridian Project for the support fund. We thank Madrigal database for inversion FPI temperature data and Google Earth for the earth picture. We are also grateful to the anonymous reviewers for their constructive comments and suggestions to improve this manuscript.

Conflicts of Interest: The authors declare no conflict of interest.

Appendix A

Table A1. Comparative data of inversion temperature and FPI temperature calculated with \overline{m}_0 in 2014.

Name and Location of FPI Stations	DOY	UT, h	LT, h	Location of Swarm B, °	Average Location, °	ALT-B, km	Average ALT, km	Temperature of FPI, k	Temperature of Swarm, k
				Location of Swarm A/C, °		ALT-A/C, km			
Arecibo (18.34°, -66.75°)	112	5.4500	1.3837	16.30, -62 15.39 -59.99	15.85, -61	515.66 468.33	492	1088.68	887.57
	112	5.4542	1.3392	17.66, -63.46 15.39 -59.99	16.53, -61.73	515.66 468.35	492.01	1088.73	837.66
	112	5.4542	1.3385	15.73, -63.43 17.29, -60.04	16.51, -61.74	515.67 468.33	492	1088.73	894.91
	112	5.4542	1.3862	16.3, -62 17.29, -60.04	16.8, -61.02	515.67 468.33	492	1088.73	922.71
	112	5.4583	1.3417	17.66, -63.46 17.29, -60.04	17.48, -61.75	515.67 468.35	492.01	1088.77	868.91
	112	5.4583	1.3893	18.22, -62.03 17.29, -60.04	17.76, -61.04	515.67 468.36	492.02	1088.77	893.26
	112	5.4625	1.3448	19.58, -63.49 17.29, -60.04	18.44, -61.77	515.67 468.4	492.04	1088.82	843.63
	112	5.4625	1.3445	17.66, -63.46 19.2, -60.08	18.43, -61.77	515.71 468.35	492.03	1088.82	903.36
	112	5.4625	1.3922	18.22, -62.03 19.2, -60.08	18.71, -61.06	515.71 468.36	492.04	1088.82	929.69
	112	5.4667	1.3477	19.58, -63.49 19.2, -60.08	19.39, -61.79	515.71 468.4	492.06	1088.86	876.11
	112	5.4667	1.3953	20.15, -62.06 19.2, -60.08	19.68, -61.07	515.71 468.43	492.07	1088.86	898.58
	112	5.4708	1.3512	21.51, -63.51 19.2, -60.08	20.36, -61.8	515.71 468.49	492.1	1088.9	849.12
	112	5.4708	1.3505	19.58, -63.49 21.1, -60.12	20.34, -61.81	515.79 468.4	492.1	1088.9	912.78
	112	5.4708	1.3982	20.15, -62.06 21.1, -60.12	20.63, -61.09	515.71 468.43	492.11	1088.9	937.18

Table A1. Cont.

Name and Location of FPI Stations	DOY	UT, h	LT, h	Location of Swarm B, °	Average Location, °	ALT-B, km	Average ALT, km	Temperature of FPI, k	Temperature of Swarm, k
				Location of Swarm A/C, °		ALT-A/C, km			
Easter Kentucky (37.75°, -84.29°)	143	3.8583	22.6973	34.74, -80.55 35.93, -74.28	35.34, -77.42	517.39 468.65	493.02	1038.31	1063.6
	143	3.8625	22.7018	36.66, -80.54 35.93, -74.28	36.3, -77.41	517.39 468.97	493.18	1038.62	1037.24
	143	3.8667	22.7057	36.66, -80.54 37.83, -74.29	37.25, -77.42	517.73 468.97	493.35	1038.48	1062.43
	143	3.8708	22.7105	38.58, -80.52 37.83, -74.29	38.21, -77.41	517.73 469.31	493.52	1038.34	1035.98
	143	3.875	22.7147	38.58, -80.52 39.73, -74.29	39.16, -77.41	518.09 469.31	493.7	1038.2	1060.56
	143	3.8792	22.7195	40.5, -80.5 39.73, -74.29	40.12, -77.4	518.09 469.66	493.88	1038.06	1034.47
	168	2.0542	20.5625	34.51, -85.29 36.34, -79.46	35.43, -82.38	517.96 468.57	493.27	1081.03	944.58
	168	2.0542	20.5632	36.43, -85.28 34.44, -79.45	35.44, -82.37	517.65 468.89	493.27	1081.03	903.84
	168	2.0583	20.5183	35.67, -86.74 36.34, -79.46	36.01, -83.1	517.96 468.74	493.35	1081.15	910.72
	168	2.0583	20.567	36.43, -85.28 36.34, -79.46	36.39, -82.37	517.96 468.89	493.43	1081.15	926.49
	168	2.0625	20.5232	37.59, -86.72 36.34, -79.46	36.97, -83.09	517.96 469.07	493.52	1081.2	893.85
	168	2.0625	20.5708	36.43, -85.28 38.24, -79.47	37.34, -82.38	518.28 468.89	493.59	1081.2	949.9
	168	2.0625	20.5715	38.35, -85.27 36.34, -79.46	37.35, -82.37	517.96 469.22	493.59	1081.2	909.78
	168	2.0667	20.527	37.59, -86.72 38.24, -79.47	37.92, -83.1	518.28 469.07	493.68	1081.25	915.91
	168	2.0667	20.5753	38.35, -85.27 38.24, -79.47	38.3, -82.37	518.28 469.22	493.75	1081.25	932.6
	168	2.0708	20.5318	39.51, -86.7 38.24, -79.47	38.88, -83.09	518.28 469.41	493.85	1081.3	898.69
	168	2.0708	20.5795	38.35, -85.27 40.14, -79.47	39.25, -82.37	518.62 469.22	493.92	1081.3	955.56
	168	2.0708	20.5802	40.27, -85.25 38.24, -79.47	39.26, -82.36	518.28 469.57	493.93	1081.3	915.65
	168	2.075	20.536	39.51, -86.7 40.14, -79.47	39.83, -83.09	518.62 469.41	494.02	1081.34	920.31
	168	2.075	20.5844	40.27, -85.25 40.14, -79.47	40.21, -82.36	518.62 469.57	494.1	1081.34	938.06
	174	2.0875	20.0379	35.28, -94.18 35.86, -87.31	35.57, -90.75	517.65 468.67	493.16	990.56	920.98
	174	2.0917	20.0417	35.28, -94.18 37.76, -87.32	36.52, -90.75	517.97 468.67	493.32	990.68	930.27
	174	2.0917	20.0424	37.2, -94.17 35.86, -87.31	36.53, -90.74	517.65 468.99	493.32	990.68	910.9
	174	2.0958	20.0462	37.2, -94.17 37.76, -87.32	37.48, -90.75	517.97 468.99	493.48	990.88	920.11

Table A1. Cont.

Name and Location of FPI Stations	DOY	UT, h	LT, h	Location of Swarm B, °	Average Location, °	ALT-B, km	Average ALT, km	Temperature of FPI, k	Temperature of Swarm, k
				Location of Swarm A/C, °		ALT-A/C, km			
Easter Kentucky (37.75°, -84.29°)	174	2.1	20.05	37.2, -94.17 39.66, -87.33	38.43, -90.75	518.3 468.99	493.65	991.08	928.83
	174	2.1	20.0507	39.12, -94.16 37.76, -87.32	38.44, -90.74	517.97 469.33	493.65	991.08	910.08
	174	2.1042	20.0545	39.12, -94.16 39.66, -87.33	39.39, -90.75	518.3 469.33	493.82	991.27	918.73
Peach mountain (42.27°, -83.75°)	168	2.0958	20.5602	43.35, -86.64 45.83, -79.43	44.59, -83.04	519.7 470.13	494.92	1036.22	949.87
	168	2.0958	20.5609	45.26, -86.59 43.93, -79.46	44.6, -83.03	519.33 470.51	494.92	1036.22	912.71
	174	2.125	20.0787	42.95, -94.1 45.35, -87.29	44.15, -90.7	519.35 470.04	494.7	914.79	920.76
	174	2.125	20.0797	44.87, -94.05 43.45, -87.31	44.16, -90.68	518.99 470.41	494.7	914.79	905.27
Pisgah (35.2°, -82.85°)	112	7.1	1.3897	33.11, -87.17 32.64, -84.14	32.88, -85.66	516.91 469.65	493.28	898.09	1001.83
	112	7.1	1.4377	33.67, -85.73 32.64, -84.14	33.16, -84.94	516.91 469.74	493.33	898.09	991.8
	112	7.1042	1.3938	35.03, -87.17 32.64, -84.14	33.84, -85.66	516.91 469.94	493.43	898.36	965.39
	112	7.1042	1.3932	33.11, -87.17 34.54, -84.16	33.83, -85.67	517.18 469.65	493.42	898.36	1044.64
	112	7.1042	1.4412	33.67, -85.73 34.54, -84.16	34.11, -84.95	517.18 469.74	493.46	898.36	1033.88
	112	7.1083	1.3973	35.03, -87.17 34.54, -84.16	34.79, -85.67	517.18 469.94	493.56	898.29	1005.55
	112	7.1083	1.4453	35.59, -85.73 34.54, -84.16	35.07, -84.95	517.18 470.03	493.61	898.29	994.54
	112	7.1125	1.4018	36.95, -87.16 34.54, -84.16	35.75, -85.66	517.18 470.24	493.71	898.22	968.96
	112	7.1125	1.4012	35.03, -87.17 36.44, -84.17	35.74, -85.67	517.48 469.94	493.71	898.22	1048.81
	112	7.1125	1.4492	35.59, -85.73 36.44, -84.17	36.02, -84.95	517.48 470.03	493.76	898.22	1037
	112	7.1167	1.4057	36.95, -87.16 36.44, -84.17	36.7, -85.67	517.48 470.24	493.86	898.15	1009.58
	112	7.1167	1.4537	37.51, -85.72 36.44, -84.17	36.98, -84.95	517.48 470.34	493.91	898.15	997.47
	112	7.1208	1.4105	38.87, -87.14 36.44, -84.17	37.66, -85.66	517.48 470.57	494.03	898.08	972.57
	112	7.1208	1.4095	36.95, -87.16 38.34, -84.18	37.65, -85.67	517.79 470.24	494.02	898.08	1053.3
	143	3.8458	22.7335	31.54, -79.11 34.03, -74.26	32.79, -76.69	517.06 468.17	492.62	893.31	1076.3
	143	3.8458	22.7342	33.46, -79.11 32.13, -74.24	32.8, -76.68	516.76 468.45	492.61	893.31	1025.52
143	3.85	22.6897	32.82, -80.55 34.03, -74.26	33.43, -77.41	517.06 468.35	492.71	893.05	1064.71	

Table A1. Cont.

Name and Location of FPI Stations	DOY	UT, h	LT, h	Location of Swarm B, °	Average Location, °	ALT-B, km	Average ALT, km	Temperature of FPI, k	Temperature of Swarm, k
				Location of Swarm A/C, °		ALT-A/C, km			
Pisgah (35.2°, -82.85°)	143	3.85	22.7377	33.46, -79.11 34.03, -74.26	33.75, -76.69	517.06 468.45	492.76	893.05	1049.78
	143	3.8542	22.6938	34.74, -80.55 34.03, -74.26	34.39, -77.41	517.06 468.65	492.86	892.78	1038.25
	143	3.8542	22.7411	33.46, -79.11 35.93, -74.28	34.7, -76.7	517.39 468.45	492.92	892.78	1075.51
	143	3.8542	22.7422	35.38, -79.1 34.03, -74.26	34.71, -76.68	517.06 468.76	492.91	892.78	1023.8
	143	3.8583	22.6973	34.74, -80.55 35.93, -74.28	35.34, -77.42	517.39 468.65	493.02	891.82	1063.6
	143	3.8583	22.7456	35.38, -79.1 35.93, -74.28	35.66, -76.69	517.39 468.76	493.08	891.82	1048.6
	143	3.8625	22.7018	36.66, -80.54 35.93, -74.28	36.3, -77.41	517.39 468.97	493.18	891.57	1037.24
	143	3.8625	22.7495	35.38, -79.1 37.83, -74.29	36.61, -76.7	517.73 468.76	493.25	891.57	1074.14
	143	3.8625	22.7501	37.3, -79.09 35.93, -74.28	36.62, -76.69	517.39 469.08	493.24	891.57	1022.68
	143	3.8667	22.7057	36.66, -80.54 37.83, -74.29	37.25, -77.42	517.73 468.97	493.35	891.32	1062.43
	143	3.8667	22.754	37.3, -79.09 37.83, -74.29	37.57, -76.69	517.73 469.08	493.41	891.32	1047.32
	168	2.0458	20.5069	33.75, -86.74 32.54, -79.43	33.15, -83.09	517.36 468.43	492.9	1000.05	883.9
	168	2.0458	20.5545	32.59, -85.29 34.44, -79.45	33.52, -82.37	517.65 468.28	492.97	1000.05	939.43
	168	2.0458	20.5551	34.51, -85.29 32.54, -79.43	33.53, -82.36	517.36 468.57	492.97	1000.05	898.59
	168	2.05	20.5104	33.75, -86.74 34.44, -79.45	34.1, -83.1	517.65 468.43	493.04	999.8	905.9
	168	2.05	20.5587	34.51, -85.29 34.44, -79.45	34.48, -82.37	517.65 468.57	493.11	999.8	921.31
	168	2.0542	20.5145	35.67, -86.74 34.44, -79.45	35.06, -83.1	517.65 468.74	493.2	999.22	888.8
	168	2.0542	20.5625	34.51, -85.29 36.34, -79.46	35.43, -82.38	517.96 468.57	493.27	999.22	944.58
	168	2.0542	20.5632	36.43, -85.28 34.44, -79.45	35.44, -82.37	517.65 468.89	493.27	999.22	903.84
	168	2.0583	20.5183	35.67, -86.74 36.34, -79.46	36.01, -83.1	517.96 468.74	493.35	998.98	910.72
	168	2.0583	20.567	36.43, -85.28 36.34, -79.46	36.39, -82.37	517.96 468.89	493.43	998.98	926.49
	168	2.0625	20.5232	37.59, -86.72 36.34, -79.46	36.97, -83.09	517.96 469.07	493.52	998.73	893.85
	168	2.0625	20.5708	36.43, -85.28 38.24, -79.47	37.34, -82.38	518.28 468.89	493.59	998.73	949.9
	168	2.0625	20.5715	38.35, -85.27 36.34, -79.46	37.35, -82.37	517.96 469.22	493.59	998.73	909.78

Table A1. Cont.

Name and Location of FPI Stations	DOY	UT, h	LT, h	Location of Swarm B, °	Average Location, °	ALT-B, km	Average ALT, km	Temperature of FPI, k	Temperature of Swarm, k
				Location of Swarm A/C, °		ALT-A/C, km			
Urbana (40.13°, -88.2°)	112	7.1208	1.4105	38.87, -87.14	37.66, -85.66	517.48	494.03	994.39	972.57
				36.44, -84.17		470.57			
	112	7.1208	1.4095	36.95, -87.16	37.65, -85.67	517.79	494.02	994.39	1053.3
				38.34, -84.18		470.24			
	112	7.1208	1.4575	37.51, -85.72	37.93, -84.95	517.79	494.07	994.39	1040.3
				38.34, -84.18		470.34			
	112	7.125	1.4143	38.87, -87.14	38.61, -85.66	517.79	494.18	993.78	1013.64
				38.34, -84.18		470.57			
	112	7.125	1.4623	39.43, -85.7	38.89, -84.94	517.79	494.23	993.78	1000.54
				38.34, -84.18		470.67			
	112	7.1292	1.4192	40.78, -87.12	39.56, -85.65	517.79	494.35	993.74	977.73
				38.34, -84.18		470.9			
	112	7.1292	1.4185	38.87, -87.14	39.56, -85.66	518.12	494.35	993.74	1056.14
				40.24, -84.18		470.57			
	112	7.1292	1.4665	39.43, -85.7	39.84, -84.94	518.12	494.4	993.74	1042.11
				40.24, -84.18		470.67			
	112	7.1333	1.4233	40.78, -87.12	40.51, -85.65	518.12	494.51	993.7	1017.76
				40.24, -84.18		470.9			
	112	7.1333	1.4717	41.34, -85.67	40.79, -84.93	518.12	494.57	993.7	1002.4
				40.24, -84.18		471.01			
	112	7.1375	1.4288	42.7, -87.08	41.47, -85.63	518.12	494.69	993.66	982.72
				40.24, -84.18		471.25			
	112	7.1375	1.4278	40.78, -87.12	41.46, -85.65	518.47	494.69	993.66	1059.24
				42.14, -84.17		470.9			
	112	7.1375	1.4762	41.34, -85.67	41.74, -84.92	518.47	494.74	993.66	1042.83
				42.14, -84.17		471.01			
	112	7.1417	1.4333	42.7, -87.08	42.42, -85.63	518.47	494.86	993.46	1021.89
				42.14, -84.17		471.25			
137	5.3958	23.2755	38.97, -93.49	37.8, -91.81	517.17	493.29	996.4	1018.72	
			36.63, -90.12		469.4				
137	5.3958	23.2749	37.05, -93.5	37.79, -91.82	517.52	493.29	996.4	1095.5	
			38.53, -90.13		469.06				
137	5.4	23.2314	38.36, -94.93	38.45, -92.53	517.52	493.42	996.24	1055.53	
			38.53, -90.13		469.31				
137	5.4	23.2794	38.97, -93.49	38.75, -91.81	517.52	493.46	996.24	1056.11	
			38.53, -90.13		469.4				
137	5.4042	23.2362	40.28, -94.91	39.41, -92.52	517.52	493.59	996.01	1021.46	
			38.53, -90.13		469.66				
137	5.4042	23.2355	38.36, -94.93	39.4, -92.53	517.89	493.6	996.01	1094.6	
			40.43, -90.13		469.31				
137	5.4042	23.2845	40.88, -93.46	39.71, -91.8	517.52	493.64	996.01	1019.53	
			38.53, -90.13		469.75				
137	5.4042	23.2835	38.97, -93.49	39.7, -91.81	517.89	493.65	996.01	1095.3	
			40.43, -90.13		469.4				
137	5.4083	23.2404	40.28, -94.91	40.36, -92.52	517.89	493.78	995.85	1058.55	
			40.43, -90.13		469.66				
137	5.4083	23.2887	40.88, -93.46	40.66, -91.8	517.89	493.82	995.85	1056.57	
			40.43, -90.13		469.75				

Table A1. Cont.

Name and Location of FPI Stations	DOY	UT, h	LT, h	Location of Swarm B, °	Average Location, °	ALT-B, km	Average ALT, km	Temperature of FPI, k	Temperature of Swarm, k
				Location of Swarm A/C, °		ALT-A/C, km			
Urbana (40.13°, -88.2°)	137	5.4125	23.2455	42.2, -94.88	41.32, -92.51	517.89	493.96	995.7	1025.08
				40.43, -90.13		470.02			
	137	5.4125	23.2445	40.28, -94.91	41.31, -92.52	518.26	493.96	995.7	1096.58
				42.33, -90.13		469.66			
	137	5.4125	23.2939	42.8, -93.43	41.62, -91.78	517.89	494.01	995.7	1019.87
				40.43, -90.13		470.12			
	137	5.4125	23.2928	40.88, -93.46	41.61, -91.8	518.26	494.01	995.7	1094.54
				42.33, -90.13		469.75			
	137	5.4167	23.2497	42.2, -94.88	42.27, -92.51	518.26	494.14	995.54	1061.25
				42.33, -90.13		470.02			
	137	5.4167	23.298	42.8, -93.43	42.57, -91.78	518.26	494.19	995.54	1055.78
				42.33, -90.13		470.12			
	156	3.5667	21.5716	38.77, -92.34	37.78, -89.93	517.8	493.57	934.33	874.53
				36.78, -87.51		469.33			
	156	3.5708	21.5759	38.77, -92.34	38.72, -89.93	518.15	493.74	933.98	894.65
				38.67, -87.51		469.33			
156	3.5708	21.6245	39.5, -90.88	39.09, -89.2	518.15	493.8	933.98	897.76	
			38.67, -87.51		469.45				
156	3.575	21.581	40.69, -92.31	39.68, -89.91	518.15	493.92	933.57	877.68	
			38.67, -87.51		469.69				
156	3.5792	21.5852	40.69, -92.31	40.63, -89.91	518.51	494.1	933.16	897.64	
			40.57, -87.51		469.69				
156	3.5792	21.6339	41.42, -90.85	41, -89.18	518.51	494.17	933.16	900.69	
			40.57, -87.51		469.82				
156	3.5833	21.5904	42.61, -92.28	41.59, -89.9	518.51	494.29	932.75	881.13	
			40.57, -87.51		470.06				
156	3.5875	21.5945	42.61, -92.28	42.54, -89.9	518.88	494.47	932.34	900.72	
			42.47, -87.51		470.06				
Virginia (37.2°, -80.42°)	112	7.1083	1.3973	35.03, -87.17	34.79, -85.67	469.94	493.56	997.97	1005.55
				34.54, -84.16		493.56			
	112	7.1083	1.4453	35.59, -85.73	35.07, -84.95	470.03	493.61	997.97	994.54
				34.54, -84.16		493.61			
	112	7.1125	1.4018	36.95, -87.16	35.75, -85.66	470.24	493.71	997.55	968.96
				34.54, -84.16		493.71			
	112	7.1125	1.4012	35.03, -87.17	35.74, -85.67	469.94	493.71	997.55	1048.81
				36.44, -84.17		493.71			
	112	7.1125	1.4492	35.59, -85.73	36.02, -84.95	470.03	493.76	997.55	1037
				36.44, -84.17		493.76			
	112	7.1167	1.4057	36.95, -87.16	36.7, -85.67	470.24	493.86	997.57	1009.58
				36.44, -84.17		493.86			
	112	7.1167	1.4537	37.51, -85.72	36.98, -84.95	470.34	493.91	997.57	997.47
				36.44, -84.17		493.91			
	112	7.1208	1.4105	38.87, -87.14	37.66, -85.66	470.57	494.03	997.59	972.57
				36.44, -84.17		494.03			
112	7.1208	1.4095	36.95, -87.16	37.65, -85.67	470.24	494.02	997.59	1053.3	
			38.34, -84.18		494.02				
112	7.1208	1.4575	37.51, -85.72	37.93, -84.95	470.34	494.07	997.59	1040.3	
			38.34, -84.18		494.07				

Table A1. Cont.

Name and Location of FPI Stations	DOY	UT, h	LT, h	Location of Swarm B, °	Average Location, °	ALT-B, km	Average ALT, km	Temperature of FPI, k	Temperature of Swarm, k
				Location of Swarm A/C, °		ALT-A/C, km			
Virginia (37.2°, -80.42°)	112	7.125	1.4143	38.87, -87.14	38.61, -85.66	470.57	494.18	998.09	1013.64
				38.34, -84.18		494.18			
	112	7.125	1.4623	39.43, -85.7	38.89, -84.94	470.67	494.23	998.09	1000.54
				38.34, -84.18		494.23			
	112	7.1292	1.4192	40.78, -87.12	39.56, -85.65	470.9	494.35	998.11	977.73
				38.34, -84.18		494.35			
	112	7.1292	1.4185	38.87, -87.14	39.56, -85.66	470.57	494.35	998.11	1056.14
				40.24, -84.18		494.35			
	143	3.8583	22.6973	34.74, -80.55	35.34, -77.42	468.65	493.02	984.75	1063.6
				35.93, -74.28		493.02			
	143	3.8583	22.7456	35.38, -79.1	35.66, -76.69	468.76	493.08	984.75	1048.6
				35.93, -74.28		493.08			
	143	3.8625	22.7018	36.66, -80.54	36.3, -77.41	468.97	493.18	984.66	1037.24
				35.93, -74.28		493.18			
	143	3.8625	22.7495	35.38, -79.1	36.61, -76.7	468.76	493.25	984.66	1074.14
				37.83, -74.29		493.25			
	143	3.8625	22.7501	37.3, -79.09	36.62, -76.69	469.08	493.24	984.66	1022.68
				35.93, -74.28		493.24			
	143	3.8667	22.7057	36.66, -80.54	37.25, -77.42	468.97	493.35	984.57	1062.43
				37.83, -74.29		493.35			
	143	3.8667	22.754	37.3, -79.09	37.57, -76.69	469.08	493.41	984.57	1047.32
				37.83, -74.29		493.41			
	143	3.8708	22.7105	38.58, -80.52	38.21, -77.41	469.31	493.52	984.48	1035.98
				37.83, -74.29		493.52			
	143	3.8708	22.7582	37.3, -79.09	38.52, -76.69	469.08	493.59	984.48	1072.23
				39.73, -74.29		493.59			
	143	3.8708	22.7585	39.22, -79.08	38.53, -76.69	469.43	493.58	984.48	1021.35
				37.83, -74.29		493.58			
	143	3.875	22.7147	38.58, -80.52	39.16, -77.41	469.31	493.7	984.39	1060.56
				39.73, -74.29		493.7			
143	3.875	22.7627	39.22, -79.08	39.48, -76.69	469.43	493.76	984.39	1045.4	
			39.73, -74.29		493.76				
162	2.0167	21.0857	34.53, -76.35	34.92, -73.97	468.71	493.24	1048.98	980.04	
			35.3, -71.58		493.24				
162	2.0208	21.0418	35.67, -77.79	35.49, -74.69	468.87	493.32	1048.52	957.52	
			35.3, -71.58		493.32				
162	2.0208	21.0902	36.45, -76.34	35.88, -73.96	469.03	493.4	1048.52	958.83	
			35.3, -71.58		493.4				
162	2.025	21.0463	37.58, -77.78	36.44, -74.68	469.2	493.48	1048.2	937.99	
			35.3, -71.58		493.48				
162	2.025	21.0457	35.67, -77.79	36.44, -74.69	468.87	493.48	1048.2	982.09	
			37.2, -71.59		493.48				
162	2.025	21.094	36.45, -76.34	36.83, -73.97	469.03	493.56	1048.2	983.54	
			37.2, -71.59		493.56				
162	2.0292	21.0502	37.58, -77.78	37.39, -74.69	469.2	493.64	1047.88	961.85	
			37.2, -71.59		493.64				
162	2.0292	21.0989	38.36, -76.32	37.78, -73.96	469.36	493.72	1047.88	962.74	
			37.2, -71.59		493.72				

Table A1. Cont.

Name and Location of FPI Stations	DOY	UT, h	LT, h	Location of Swarm B, °	Average Location, °	ALT-B, km	Average ALT, km	Temperature of FPI, k	Temperature of Swarm, k
				Location of Swarm A/C, °		ALT-A/C, km			
Virginia (37.2°, −80.42°)	162	2.0333	21.055	39.5, −77.76	38.35, −74.68	469.55	493.82	1047.56	942.48
				37.2, −71.59		493.82			
	162	2.0333	21.054	37.58, −77.78	38.34, −74.69	469.2	493.81	1047.56	986.25
				39.1, −71.6		493.81			
	162	2.0333	21.1027	38.36, −76.32	38.73, −73.96	469.36	493.89	1047.56	987.27
				39.1, −71.6		493.89			
	162	2.0375	21.0589	39.5, −77.76	39.3, −74.68	469.55	493.99	1047.25	966.22
				39.1, −71.6		493.99			
	162	2.0375	21.1075	40.28, −76.3	39.69, −73.95	469.71	494.07	1047.25	966.66
				39.1, −71.6		494.07			
	168	2.0542	20.5145	35.67, −86.74	35.06, −83.1	468.74	493.2	1023.73	888.8
				34.44, −79.45		493.2			
	168	2.0542	20.5625	34.51, −85.29	35.43, −82.38	468.57	493.27	1023.73	944.58
				36.34, −79.46		493.27			
	168	2.0542	20.5632	36.43, −85.28	35.44, −82.37	468.89	493.27	1023.73	903.84
				34.44, −79.45		493.27			
	168	2.0583	20.5183	35.67, −86.74	36.01, −83.1	468.74	493.35	1023.57	910.72
				36.34, −79.46		493.35			
	168	2.0583	20.567	36.43, −85.28	36.39, −82.37	468.89	493.43	1023.57	926.49
				36.34, −79.46		493.43			
168	2.0625	20.5232	37.59, −86.72	36.97, −83.09	469.07	493.52	1023.42	893.85	
			36.34, −79.46		493.52				
168	2.0625	20.5708	36.43, −85.28	37.34, −82.38	468.89	493.59	1023.42	949.9	
			38.24, −79.47		493.59				
168	2.0625	20.5715	38.35, −85.27	37.35, −82.37	469.22	493.59	1023.42	909.78	
			36.34, −79.46		493.59				
168	2.0667	20.527	37.59, −86.72	37.92, −83.1	469.07	493.68	1023.26	915.91	
			38.24, −79.47		493.68				
168	2.0667	20.5753	38.35, −85.27	38.3, −82.37	469.22	493.75	1023.26	932.6	
			38.24, −79.47		493.75				
168	2.0708	20.5318	39.51, −86.7	38.88, −83.09	469.41	493.85	1022.9	898.69	
			38.24, −79.47		493.85				
168	2.0708	20.5795	38.35, −85.27	39.25, −82.37	469.22	493.92	1022.9	955.56	
			40.14, −79.47		493.92				
168	2.0708	20.5802	40.27, −85.25	39.26, −82.36	469.57	493.93	1022.9	915.65	
			38.24, −79.47		493.93				
Xing Long (40.2°, 117.4°)	118	16.6333	0.8973	38.19, 123.23	37.88, 123.96	517.47	493.81	959.93	922.82
				37.57, 124.69		470.15			
	118	16.6375	0.8542	39.55, 121.81	38.56, 123.25	517.47	493.93	959.84	895.31
				37.57, 124.69		470.39			
	118	16.6375	0.8535	37.63, 121.79	38.55, 123.24	517.8	493.93	959.84	959.91
				39.47, 124.69		470.06			
	118	16.6375	0.9015	38.19, 123.23	38.83, 123.96	517.8	493.98	959.84	958.39
39.47, 124.69				470.15					
118	16.6417	0.8583	39.55, 121.81	39.51, 123.25	517.8	494.1	959.74	929.13	
			39.47, 124.69		470.39				
118	16.6417	0.9067	40.11, 123.26	39.79, 123.98	517.8	494.14	959.74	927.44	
			39.47, 124.69		470.48				

Table A1. Cont.

Name and Location of FPI Stations	DOY	UT, h	LT, h	Location of Swarm B, °	Average Location, °	ALT-B, km	Average ALT, km	Temperature of FPI, k	Temperature of Swarm, k
				Location of Swarm A/C, °		ALT-A/C, km			
Xing Long (40.2°, 117.4°)	118	16.6458	0.8635	41.47, 121.84 39.47, 124.69	40.47, 123.27	517.8 470.73	494.27	959.65	900.2
	118	16.6458	0.8625	39.55, 121.81 41.37, 124.69	40.46, 123.25	518.15 470.39	494.27	959.65	964.76
	118	16.6458	0.9108	40.11, 123.26 41.37, 124.69	40.74, 123.98	518.15 470.48	494.32	959.65	963.02
	118	16.65	0.8677	41.47, 121.84 41.37, 124.69	41.42, 123.27	518.15 470.73	494.44	959.56	934.08
	118	16.65	0.9157	42.03, 123.28 41.37, 124.69	41.7, 123.99	518.15 470.82	494.49	959.56	932.15
	118	16.6542	0.8732	43.38, 121.88 41.37, 124.69	42.38, 123.29	518.15 471.09	494.62	959.47	905.01
	118	16.6542	0.8722	41.47, 121.84 43.26, 124.7	42.37, 123.27	518.51 470.73	494.62	959.47	969.58
	118	16.6542	0.9202	42.03, 123.28 43.26, 124.7	42.65, 123.99	518.51 470.82	494.67	959.47	967.59
	143	14.8875	22.7149	38.39, 115.87 37.08, 118.95	37.74, 117.41	517.61 469.32	493.47	1118.16	900.95
	143	14.8917	22.6707	37.76, 114.43 38.98, 118.94	38.37, 116.69	517.96 469.22	493.59	1117.94	927.64
	143	14.8917	22.7186	38.39, 115.87 38.98, 118.94	38.69, 117.41	517.96 469.32	493.64	1117.94	930.77
	143	14.8958	22.6752	39.68, 114.44 38.98, 118.94	39.33, 116.69	517.96 469.57	493.77	1117.73	899.96
	143	14.8958	22.7235	40.31, 115.89 38.98, 118.94	39.65, 117.42	517.96 469.68	493.82	1117.73	902.19
	143	14.8958	22.7229	38.39, 115.87 40.88, 118.94	39.64, 117.41	518.33 469.32	493.83	1117.73	961.69
	143	14.9	22.6794	39.68, 114.44 40.88, 118.94	40.28, 116.69	518.33 469.57	493.95	1117.51	929.23
	143	14.9	22.7277	40.31, 115.89 40.88, 118.94	40.6, 117.42	518.33 469.68	494.01	1117.51	931.65
	143	14.9042	22.6845	41.59, 114.47 40.88, 118.94	41.24, 116.71	518.33 469.93	494.13	1117.3	902.39
	143	14.9042	22.7329	42.23, 115.92 40.88, 118.94	41.56, 117.43	518.33 470.04	494.19	1117.3	903.65
	143	14.9042	22.7322	40.31, 115.89 42.77, 118.95	41.54, 117.42	518.71 469.68	494.2	1117.3	961.81
	143	14.9083	22.689	41.59, 114.47 42.77, 118.95	42.18, 116.71	518.71 469.93	494.32	1117.09	931.03
	143	14.9083	22.7374	42.23, 115.92 42.77, 118.95	42.5, 117.44	518.71 470.04	494.38	1117.09	932.43

References

- Burke, W.J.; Lin, C.S.; Hagan, M.P.; Huang, C.Y.; Weimer, D.R.; Wise, J.O.; Gentile, L.C.; Marcos, F.A. Storm time global thermosphere: A driven-dissipative thermodynamic system. *J. Geophys. Res.-Space Phys.* **2009**, *114*, A06306. [\[CrossRef\]](#)
- Wise, J.O.; Burke, W.J.; Sutton, E.K. Globally averaged exospheric temperatures derived from CHAMP and GRACE accelerometer measurements. *J. Geophys. Res.-Space Phys.* **2012**, *117*. [\[CrossRef\]](#)
- Picone, J.M.; Hedin, A.E.; Drob, D.P.; Aikin, A.C. Nrlmsise-00 Empirical Model of the Atmosphere: Statistical Comparisons and Scientific Issues. *J. Geophys. Res.-Space Phys.* **2002**, *107*, SIA 15-1–SIA 15-16. [\[CrossRef\]](#)

4. Forbes, J.M.; Zhang, X.; Bruinsma, S.L. New perspectives on thermosphere tides: 2. Penetration to the upper thermosphere. *Earth Planets Space* **2014**, *66*, 1–11. [[CrossRef](#)]
5. Weimer, D.R.; Sutton, E.K.; Mlynczak, M.G.; Hunt, L.A. Intercalibration of neutral density measurements for mapping the thermosphere. *J. Geophys. Res. Space Phys.* **2016**, *121*, 5975–5990. [[CrossRef](#)]
6. Weng, L.; Lei, J.; Sutton, E.; Dou, X.; Fang, H. An exospheric temperature model from CHAMP thermospheric density. *Space Weather* **2017**, *15*, 343–351. [[CrossRef](#)]
7. Evans, J.S.; Lumpe, J.D.; Correira, J.; Veibell, V.; Kyrwonos, A.; McClintock, W.E.; Solomon, S.C.; Eastes, R.W. Neutral Exospheric Temperatures From the GOLD Mission. *J. Geophys. Res.-Space Phys.* **2020**, *125*, e2020JA027814. [[CrossRef](#)]
8. Friis-Christensen, E.; Luhr, H.; Knudsen, D.; Haagmans, R. Swarm—An Earth Observation Mission investigating Geospace. *Adv. Space Res.* **2008**, *41*, 210–216. [[CrossRef](#)]
9. Doornbos, E.; van den Ijssel, J.; Luhr, H.; Forster, M.; Koppenwallner, G. Neutral Density and Crosswind Determination from Arbitrarily Oriented Multiaxis Accelerometers on Satellites. *J. Spacecr. Rockets* **2010**, *47*, 580–589. [[CrossRef](#)]
10. Van den Ijssel, J.; Doornbos, E.; Iorfida, E.; March, G.; Siemes, C.; Montenbruck, O. Thermosphere densities derived from Swarm GPS observations. *Adv. Space Res.* **2020**, *65*, 1758–1771. [[CrossRef](#)]
11. Yuan, W.; Xu, J.; Ma, R.; Wu, Q.; Jiang, G.; Gao, H.; Liu, X.; Chen, S. First observation of mesospheric and thermospheric winds by a Fabry-Perot interferometer in China. *Chin. Sci. Bull.* **2010**, *55*, 4046–4051. [[CrossRef](#)]
12. Yuan, W.; Liu, X.; Xu, J.; Zhou, Q.; Jiang, G.; Ma, R. FPI observations of nighttime mesospheric and thermospheric winds in China and their comparisons with HWM07. *Ann. Geophys.* **2013**, *31*, 1365–1378. [[CrossRef](#)]
13. Chen, G.-m.; Xu, J.; Wang, W.; Burns, A.G. A comparison of the effects of CIR- and CME-induced geomagnetic activity on thermospheric densities and spacecraft orbits: Statistical studies. *J. Geophys. Res. Space Phys.* **2014**, *119*, 7928–7939. [[CrossRef](#)]
14. Cai, X.; Burns, A.G.; Wang, W.; Qian, L.; Solomon, S.C.; Eastes, R.W.; Pedatella, N.; Daniell, R.E.; McClintock, W.E. The Two-Dimensional Evolution of Thermospheric $\Sigma\text{O}/\text{N}_2$ Response to Weak Geomagnetic Activity During Solar-Minimum Observed by GOLD. *Geophys. Res. Lett.* **2020**, *47*, e2020GL088838. [[CrossRef](#)]
15. Buonsanto, M.J.; Pohlman, L.M. Climatology of neutral exospheric temperature above Millstone Hill. *J. Geophys. Res.-Space Phys.* **1998**, *103*, 23381–23392. [[CrossRef](#)]